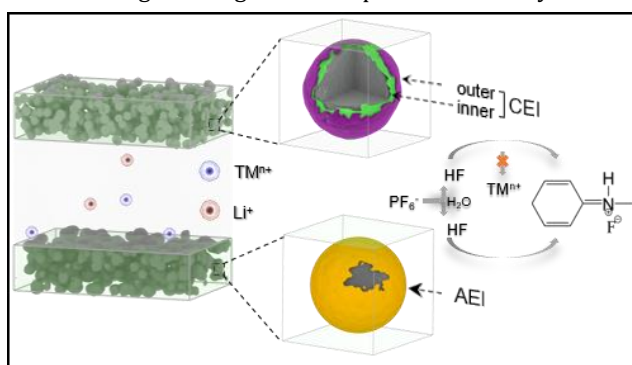


# Towards Long-life, Ultrahigh-nickel Layered Oxide Cathodes for Lithium-ion Batteries: Optimizing the Interphase Chemistry with a Dual-functional Polymer

Jianyu Li, Chi-Hao Chang, Arumugam Manthiram\*

McKetta Department of Chemical Engineering & Texas Materials Institute

**ABSTRACT:** Boosting the Ni content in  $\text{LiMO}_2$  ( $M = \text{Ni, Co, Mn, etc.}$ ) layered oxides is a promising way to establish high-energy-density, low-cost cathodes, but the poor cathode surface stability is a daunting challenge for their practical viability. Herein, by constructing a dual-functional binder framework with a conductive polymer - polyaniline (PANI), the ultrahigh-Ni layered oxide cathode ( $\text{LiNi}_{0.94}\text{Co}_{0.06}\text{O}_2$ ) exhibits significantly improved cyclability, with a capacity retention greatly increased from 47% to 81% over 1,000 cycles in full cells. It is demonstrated that the acidic species (*e.g.* HF) in the electrolyte can be efficiently scavenged through a protonation process of PANI, hence the cathode surface reactivity is greatly suppressed and the rock-salt phase propagation into bulk structure is considerably alleviated. Furthermore, the PANI binder system effectively prevents both the cathode-electrolyte interphase (CEI) and anode-electrolyte interphase (AEI) from degrading to a thick “triple-layer” architecture upon extensive cycling, resulting in more robust, thinner CEI and AEI with regulated interphasial chemistry. Moreover, the delocalized  $\pi$ -conjugated electrons along the backbone of PANI facilitate fast electron transfer and promote rate capability even at low temperatures ( $-20^\circ\text{C}$ ). This work sheds light on rational binder engineering for developing high-energy-density lithium-ion batteries with acceptable cycle life.



## 1. INTRODUCTION

In the wake of rapidly growing market for electric vehicles, advanced lithium-ion (Li-ion) batteries with higher energy density are being intensively pursued. Cathode material is the major bottleneck for achieving the high-energy-density goal. Among the contenders,  $\text{LiNiO}_2$ -based ultrahigh-Ni (Ni content  $\geq 0.9$ ) layered oxides are deemed as one of the most feasible cathode candidates owing to their high capacity and lower cost. Since the  $\text{Ni}^{3+/4+};e_g$  band barely overlaps with the top of the  $\text{O}^{2-};2p$  band, a discharge capacity of  $> 220 \text{ mA h g}^{-1}$  can be readily reached without severe oxygen loss from the lattice.<sup>1</sup> Furthermore, with a high average discharge voltage ( $\sim 3.8 \text{ V}$  vs  $\text{Li/Li}^+$ ), the ultrahigh-Ni layered oxide cathode is capable of offering a high energy density of  $> 800 \text{ Wh kg}^{-1}$  at the cathode level. Additionally, the expensive Co content is greatly reduced in ultrahigh-Ni layered oxides, which makes it a cost-effective choice for sustainable development.

Nevertheless, the practical application of ultrahigh-Ni layered oxide cathodes is hindered by their poor electrochemical cyclability, in which the cathode surface degradation plays a critical role. On one hand, the lattice oxygen becomes more nucleophilic as the Ni content increases, and the high capacity delivery in layered oxides gives rise to high-valence transition-metal ions that are highly oxidizing.<sup>2</sup> Thus, aggressive electrolyte decomposition occurs on the cathode surface, forming a cathode-electrolyte interphase (CEI) with complex surface chemistry.<sup>3</sup> On the other hand, acidic species (*e.g.*, HF) generated by  $\text{LiPF}_6$  hydrolysis attack the cathode and gradually dissolve the cathode active material.<sup>4</sup> The dissolution product migrates to the anode

side, alters the anode surface chemistry, and damages the anode-electrolyte-interphase (AEI) integrity.<sup>3</sup> Besides, electrolyte can penetrate through the microcracks created by the anisotropic lattice distortion of the ultrahigh-Ni layered oxide during repeated cycling, aggravating the cathode surface reaction.<sup>5,6</sup> Consequently, the structural degradation from the layered to rock-salt ( $\text{NiO}$ ) phases is initiated from the cathode surface and gradually propagates into the bulk particles, thus blocking Li-ion transport, causing impedance buildup, and accelerating capacity decay.<sup>7-10</sup>

Tremendous efforts have been devoted to stabilizing ultrahigh-Ni layered oxide cathodes with satisfactory cyclability,<sup>11,12</sup> and the cathode surface optimization is critical to achieve this end goal.<sup>13-15</sup> In this contribution, we present a novel strategy to prolong the cycle life of ultrahigh-Ni layered oxide cathodes ( $\text{LiNi}_{0.94}\text{Co}_{0.06}\text{O}_2$ ) by establishing a dual-functional binder framework, where a p-type conductive polymer - polyaniline (PANI) is introduced into the binder system to partially substitute the conventional binder - polyvinylidene fluoride (PVDF). First, the delocalized  $\pi$ -conjugated electrons along the backbone of PANI effectively improve the electronic conductivity of the binder framework, resulting in promoted rate capability.<sup>16</sup> Second, the imine nitrogen in PANI can be coordinated to anion groups such as  $\text{F}^-$  in the electrolyte, which scavenges acidic species like HF from  $\text{LiPF}_6$  decomposition.<sup>17</sup> Accordingly, the cathode surface reaction with electrolyte is efficiently alleviated with suppressed active-material dissolution. As a result, the CEI is regulated to a thinner dual-layer architecture, together with a minimized  $\text{NiO}$  rock salt phase formation during extensive cycling. Meanwhile, the AEI integrity is enhanced owing to the suppressed chemical crossover from t-

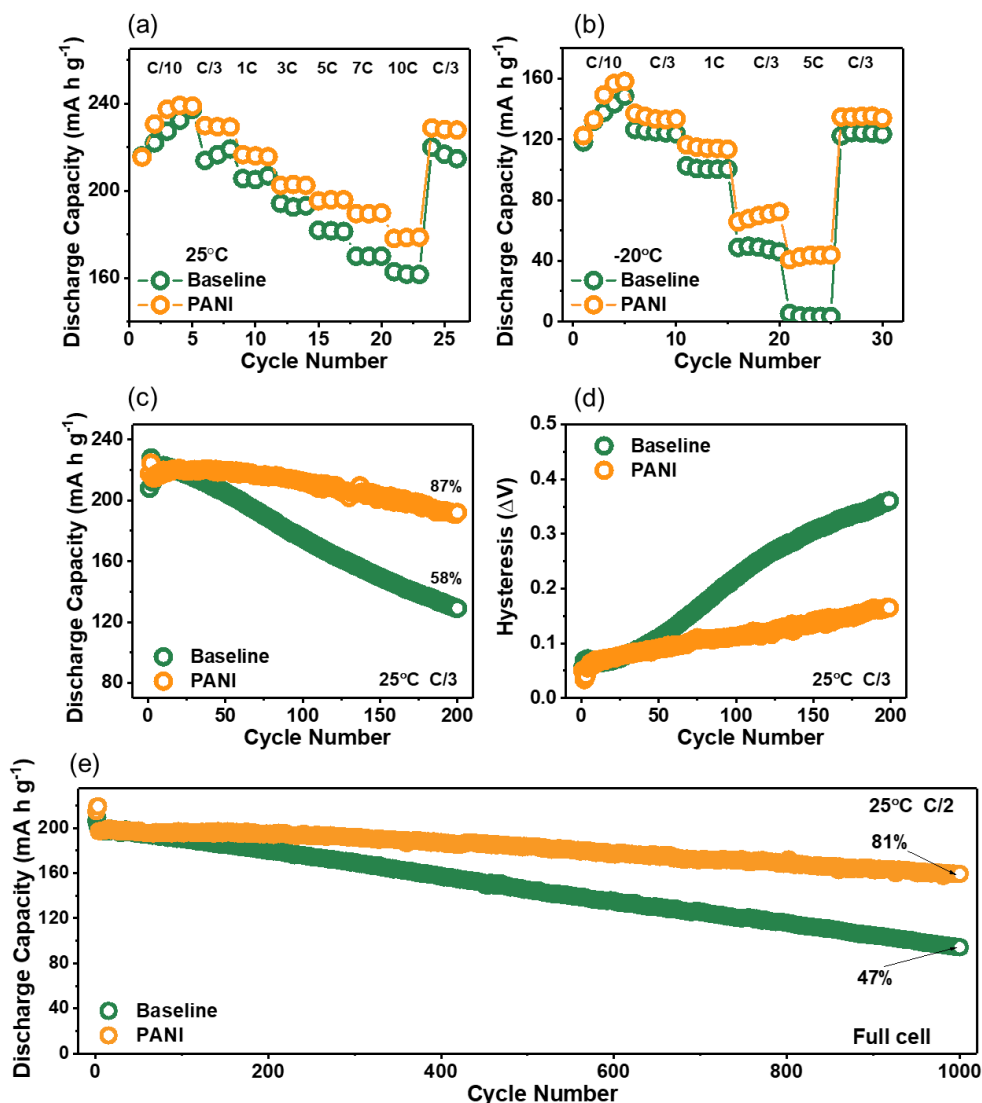


**Figure 1.** Electrochemical performance of  $\text{Li} \mid \text{LiNi}_{0.94}\text{Co}_{0.06}\text{O}_2$  half cells with different binders: rate capability at (a) 25 °C and (b) -20 °C, (c) cycling performance at C/3 rate, and (d) the corresponding voltage hysteresis evolution. (e) Cycling performance of graphite  $\mid \text{LiNi}_{0.94}\text{Co}_{0.06}\text{O}_2$  full cells with different binders.

he cathode side, and its architecture is tuned from a thick triple-layer to a thin mono-layer structure in the PANI-incorporated binder system. Collectively, the cycling performance of the ultrahigh-Ni layered oxide cathode is significantly improved, demonstrating a huge capacity-retention increase from 47% to 81% after 1,000 cycles in full cells.

## 2. RESULTS AND DISCUSSION

Figure 1a and 1b display the rate capability of half cells employing ultrahigh-Ni layered oxide cathodes ( $\text{LiNi}_{0.94}\text{Co}_{0.06}\text{O}_2$ ) with and without PANI binder (termed as, respectively, “PANI” and “baseline”) in the electrode at different temperatures. As seen, at 25 °C, due to the ultrahigh Ni content in  $\text{LiNi}_{0.94}\text{Co}_{0.06}\text{O}_2$ , both samples reach a high discharge capacity of  $\sim 240 \text{ mA h g}^{-1}$  at C/10 rate, which is one of the highest values reported for layered oxide cathodes.<sup>18</sup> As the current increases, the PANI cell outperforms the baseline cell, offering much higher discharge capacities. For instance, at 10C rate, it maintains a discharge capacity of  $179 \text{ mA h g}^{-1}$ , 11% higher than that of the baseline cell. Notably, such remarkable rate performance also extends to the

low-temperature operation. Even at -20 °C, the PANI cell still remains a capacity of  $40 \text{ mA h g}^{-1}$  at 5C rate, while the baseline cell ends up with no detectable capacity. Therefore, benefiting from the conductive PANI-incorporated binder framework, the cell demonstrates greatly facilitated electron pathway and improved rate capability.<sup>19</sup>

Figure 1c compares the cycling performance of half cells at C/3 rate. The baseline cell undergoes a fast capacity drop with only 58% retention after 200 cycles, while the PANI cell exhibits much better cycling stability (87% retention). Meanwhile, the PANI cell manifests much lower voltage hysteresis (0.16 V compared to 0.36 V in baseline cell, Figure 1d) as well as higher Coulombic efficiency (99.5% compared to 98.5% in baseline cell, Figure S2, Supporting Information). Also, the voltage plateaus at 4.2 V (corresponding to hexagonal 2 to hexagonal 3 (H2-H3) phase transition) completely vanish in the baseline cell, in sharp contrast to the well-preserved plateaus in the PANI cell (Figure S1, Supporting Information). It implies that the structural integrity is better maintained in the PANI cell. Besides the half-cell test, Figure 1e further illustrated the long-term cycling per-

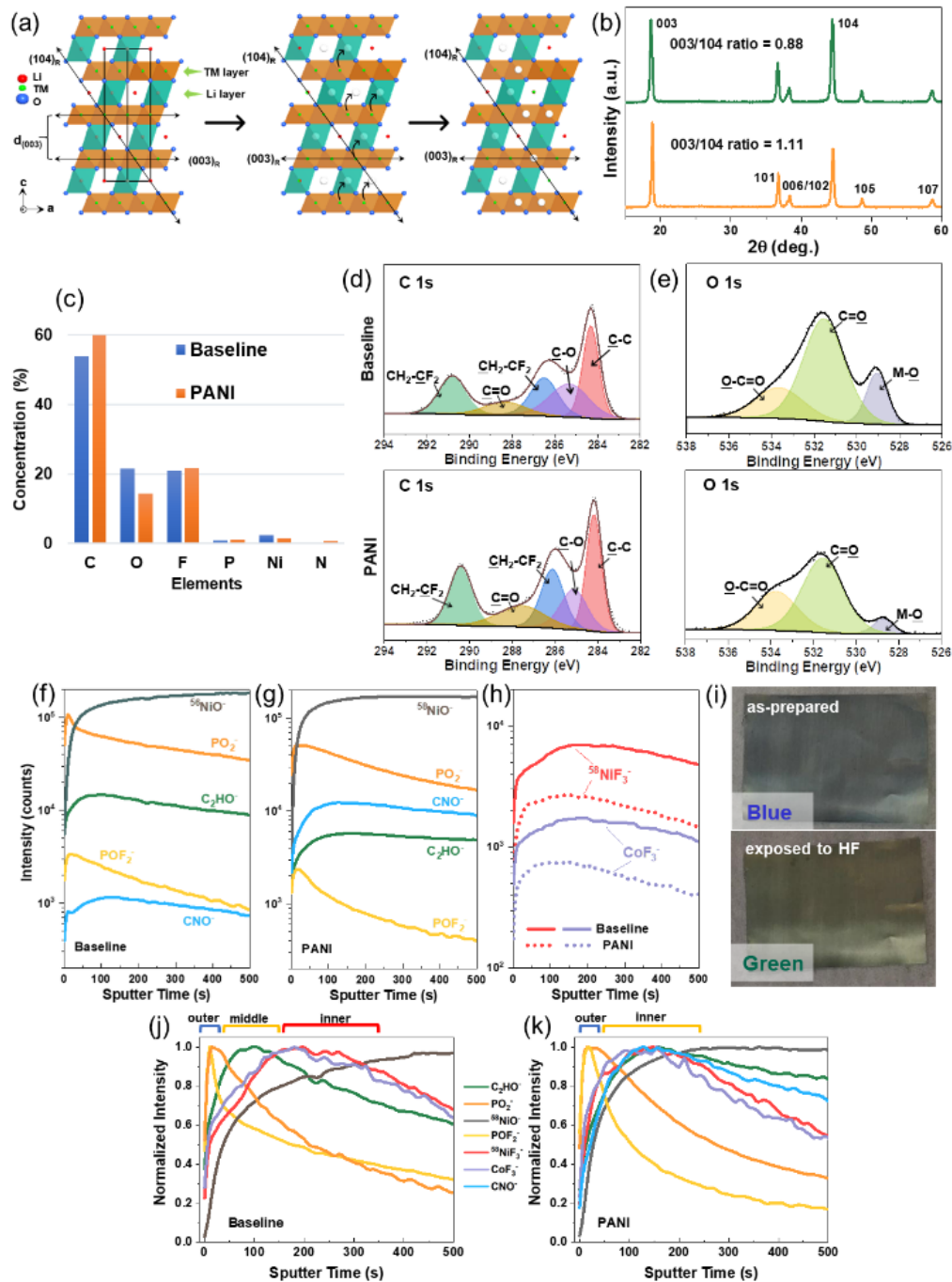


**Figure 2.** (a) Schematic illustration of the cation migration process during electrochemical cycling. Characterizations of the cycled  $\text{LiNi}_{0.94}\text{Co}_{0.06}\text{O}_2$  cathodes with different binders retrieved from full cells: (b) XRD patterns, (c) XPS surface elemental concentration, and (d) C 1s and (e) O 1s spectra. TOF-SIMS depth profiles of interphasial fragments acquired on the cycled  $\text{LiNi}_{0.94}\text{Co}_{0.06}\text{O}_2$  cathodes retrieved from full cells with (f) baseline and (g) PANI binders, and (h) comparison of the transition-metal dissolution fragments. (i) Digital image of the PANI-incorporated film before and after exposure to HF. TOF-SIMS depth profiles (normalized to maximum) of interphasial fragments for (j) baseline and (k) PANI samples illustrating the layered structure of the cathode-electrolyte interphase.

formance of full cells with  $\text{LiNi}_{0.94}\text{Co}_{0.06}\text{O}_2$  as the cathode and graphite as the anode. By employing the PANI binder in both electrodes, the full cell demonstrates a significant increase of capacity retention from 47% to 81% after 1,000 cycles (Coulombic efficiencies are shown in Figure S3, Supporting Information). In addition, the average discharge voltage drop in the full cell with PANI is greatly lowered to 0.14 V as compared to the baseline sample (0.57 V) (Figure S4, Supporting Information). More importantly, for the full cells

with PANI either on the cathode or anode side only, the capacity retention could be improved (76% retention for the full cell with PANI only on the anode side and 73% retention for the full cell with PANI only on the cathode side, Figure S5, Supporting Information). These comparisons indicate the effectiveness of PANI as the dual-function binder in improving the electrode stability, thus contributing to a great enhancement in electrochemical reversibility and long-term cyclability.

To probe the intrinsic mechanism behind the cyclability improvement, the cathode structural degradation, which is closely related to the “cation-mixing” phenomenon during electrochemical cycling, was first analyzed with X-ray diffraction (XRD).<sup>20</sup> As schematized in Figure 2a, a cation-mixed phase is formed once the transition-metal cations migrate to the adjacent vacancies in the Li layer, and it gradually evolves to a NiO rock-salt phase as the migration situation deteriorates.<sup>21</sup> Worse still, such phase transition can be aggravated once the lattice oxygen is lost during the cathode surface reaction.<sup>22</sup> Also, the degree of the structural degradation can be efficiently evaluated by looking at the intensity ratio of the (003) peak to the (104) peak in XRD.<sup>23</sup> As demonstrated in Figure 2b, after 1,000 cycles, the  $I(003)/I(104)$  ratio for the baseline sample drastically declines from 1.25 to 0.88 compared to the pristine cathode (Figure S6, Supporting Information). The PANI sample, however, still maintains a high  $I(003)/I(104)$  ratio of 1.11, suggesting a more sustained layered structure upon extensive cycling. Furthermore, the Rietveld refinement result shows the Ni occupancy in the Li layer decreases from 7% to 4% with the PANI binder in the electrode (Table S1 and S2, Supporting Information). Moreover, the material crystallinity is better preserved in the PANI sample as evidenced by the smaller full width at half maximum (FWHM) of the (003) peak. It is worth noting that the expansion of the *c* lattice implies continuous loss of Li inventory from the structure.<sup>24</sup> After 1,000 cycles, the smaller *c* lattice parameter in the PANI sample indicates a better preservation of active Li in the cathode material. Thus, it is revealed that the ultrahigh-Ni layered oxide cathode demonstrates improved crystallinity as well as structural stability, contributed by the dual-function PANI binder system over repeated cycling.

Apart from the structural degradation, cathode surface chemistry is another crucial factor for the stable cycling of the ultrahigh-Ni layered oxides. Figure 2c plots the elemental composition with X-ray photoelectron spectroscopy (XPS) characterization on the  $\text{LiNi}_{0.94}\text{Co}_{0.06}\text{O}_2$  electrodes retrieved from the 1,000 cycled full cells. The PANI sample demonstrates higher C content (mainly due to the increased C-C bonding from carbon black, Figure 2d)<sup>25</sup> as well as lower O content (arising from the declined C=O bonding, Figure 2e) than the baseline sample. It suggests that less alkyl carbonate/polycarbonate components from electrolyte decomposition are formed on the cathode surface in the PANI sample.<sup>26</sup> Additionally, the comparatively lower Ni content in the PANI sample infers better CEI coverage to minimize the transition-metal dissolution from the cathode. Note that in the PANI sample, the strong N 1s peak at 401.0 eV (Figure S7, Supporting Information) indicates the presence of the charged nitrogen coordinated to anion groups.<sup>16,17,27</sup> Interestingly, the imide groups are also detected on the cathode surface, as evidenced by the N 1s peak at 400.1 eV (Figure S7, Supporting Information), implying a slight decomposition of PANI during prolonged cycling.<sup>28</sup>

To get a deeper insight into the CEI configuration, a highly surface-sensitive technique – time-of-flight secondary ion mass spectrometry (TOF-SIMS) – was applied to unveil the cathode surface chemistry. Figure 2f – h illustrates the depth profile of the typical fragments of interest on the cycled cathodes with and without the PANI binder,

including  $\text{C}_2\text{HO}^-$  (representing organic species from electrolyte solvent decomposition),  $\text{PO}_2^-/\text{POF}_2^-$  (referring to the inorganic species from  $\text{LiPF}_6$  decomposition),  $^{58}\text{NiF}_3^-/\text{CoF}_3^-$  (representing active-material dissolution products),  $^{58}\text{NiO}^-$  (originating from the bulk cathode material), and  $\text{CNO}^-$  (stemming from the interphasial species from PANI decomposition).<sup>3</sup> As seen, the PANI sample shows much higher intensity of  $\text{CNO}^-$  fragment throughout the CEI than the baseline sample. It indicates that PANI is essentially involved in the chemical configuration of the cathode surface, and such sacrificial decomposition of PANI helps contribute to a more robust CEI.<sup>29,30</sup> Consequently, the PANI sample exhibits substantially alleviated decomposition of carbonate electrolyte solvent and  $\text{LiPF}_6$  salt due to the suppressed cathode surface reactivity, as reflected in the decreased yields of  $\text{C}_2\text{HO}^-$ ,  $\text{PO}_2^-$ , and  $\text{POF}_2^-$  fragments (Figure 2f and 2g). Additionally, the transition-metal dissolution is also effectively reduced in the PANI sample, with more than 50% decrease of  $^{58}\text{NiF}_3^-$  and  $\text{CoF}_3^-$  yields compared to the baseline sample (Figure 2h). Such mitigated cathode surface reactivity is mainly attributed to the protonation effect of PANI, which effectively scavenges the acidic species, such as HF,  $\text{PF}_3\text{O}^-$  to discourage the acidic attack on the cathode active material.<sup>31,32</sup> To better illustrate the protonation process, a thin PANI-PVDF film was prepared and cast onto an Al foil. As shown in Figure 2i, after exposing the film to the 3 wt.% HF solution for 3 s, the original blue film immediately turns green, indicating HF is coordinated to the imine nitrogen in PANI. A more detailed reaction mechanism of the protonation process is illustrated in Figure S11 (Supporting Information). Therefore, the PANI binder plays a critical role in tuning the cathode surface chemistry and suppressing the cathode surface reaction with electrolyte.

Additionally, the interphasial chemical stacking behavior throughout the CEI is further revealed with TOF-SIMS. As shown in Figure 2j and 2k, various interphasial fragments reside at different depths of the CEI, manifesting a layered architecture as cycling proceeds. For the baseline sample, the CEI is featured with a thick triple-layer architecture, where P-bearing inorganic species ( $\text{PO}_2^-/\text{POF}_2^-$ ) are located in the exterior layer, organic species from electrolyte decomposition ( $\text{C}_2\text{HO}^-$ ) dominate the intermediate layer, and the dissolved transition-metal species ( $^{58}\text{NiF}_3^-/\text{CoF}_3^-$ ) penetrate into the interior layer of the CEI. In contrast, for the PANI sample, the CEI is regulated to a thin dual-layer architecture as the exterior layer is enriched with P-bearing inorganic species, and the interior layer is dominated by both organic species and dissolved transition-metal ions. Moreover, the depth of the maximum  $^{58}\text{NiO}^-$  yield (representing bulk cathode) further reflects that the CEI thickness of the PANI sample is at least twice thinner than that of the baseline sample, as a result of significantly mitigated cathode surface reaction benefiting from the PANI binder framework.

Besides the CEI, a robust AEI is critical for efficient Li-ion intercalation into the graphite anode during repeated cycling, and it can be greatly influenced by the chemical cross-over from the cathode side.<sup>33</sup> Figure 3a – c shows the XPS data collected on the graphite anode retrieved from full cells cycled for 1,000 cycles. For the C 1s spectra, the PANI sample renders a strong C-C peak arising from the bulk graphite, implying a thin AEI after extensive cycling. In stark contrast,

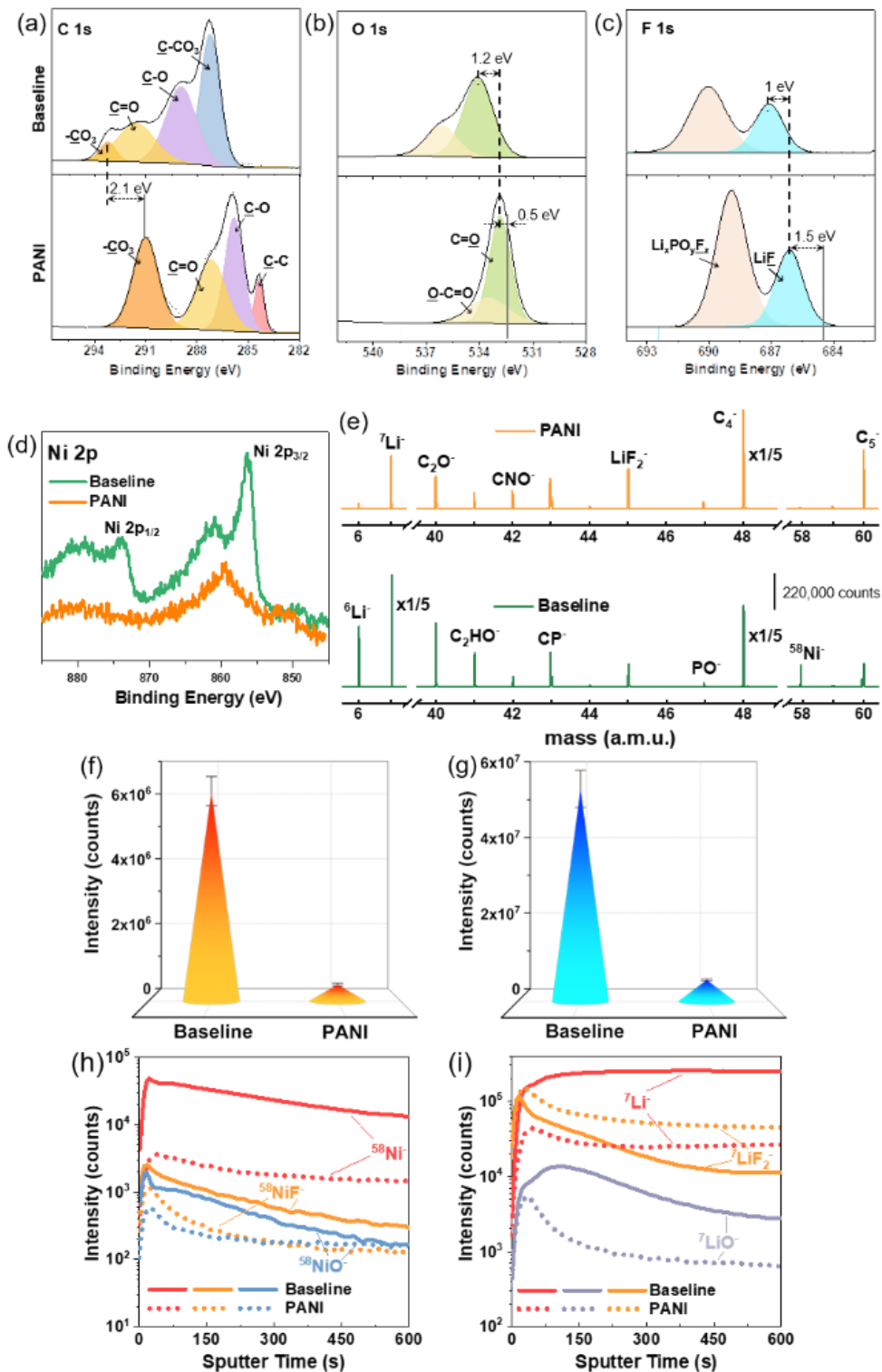


**Figure 3.** XPS characterizations on the graphite anodes retrieved from 1,000 cycled full cells: (a) C 1s, (b) O 1s, (c) F 1s, and (d) Ni 2p spectra. TOF-SIMS results on the graphite surface after 1,000 cycles: (e) intensity comparison of various fragments, the sum of the deposited (f) transition-metal (including  $^{58}\text{Ni}$ ,  $^{60}\text{Ni}$ ,  $^{61}\text{Ni}$ ,  $^{62}\text{Ni}$ , and Co) and (g) Li (including  $^6\text{Li}$  and  $^7\text{Li}$ ) yields, and depth profiles of (h) transition-metal and (i) Li-related interphasial species on the graphite surface.

the C-C peak in the baseline sample does not emerge until 30 s of Ar-sputtering (Figure S9, Supporting Information), indicative of a much thicker AEI. Interestingly, for the baseline sample, the peaks of various interphasial species demonstrate a considerable shift towards higher binding energy (*e.g.*, 2.1 eV, 1.7 eV, and 2.5 eV of positive peak shifts

for, respectively,  $-\text{CO}_3$ , C=O, and LiF species). In the case of the PANI sample, interphasial species like C=O and LiF undergo much smaller peak shifts (0.5 eV and 1.5 eV, respectively). Such a peak shift trend is attributed to the formation of metallic Li beneath the insulating species (*e.g.*, carbonates, oxides, and fluorides), where an electrostatic dou-

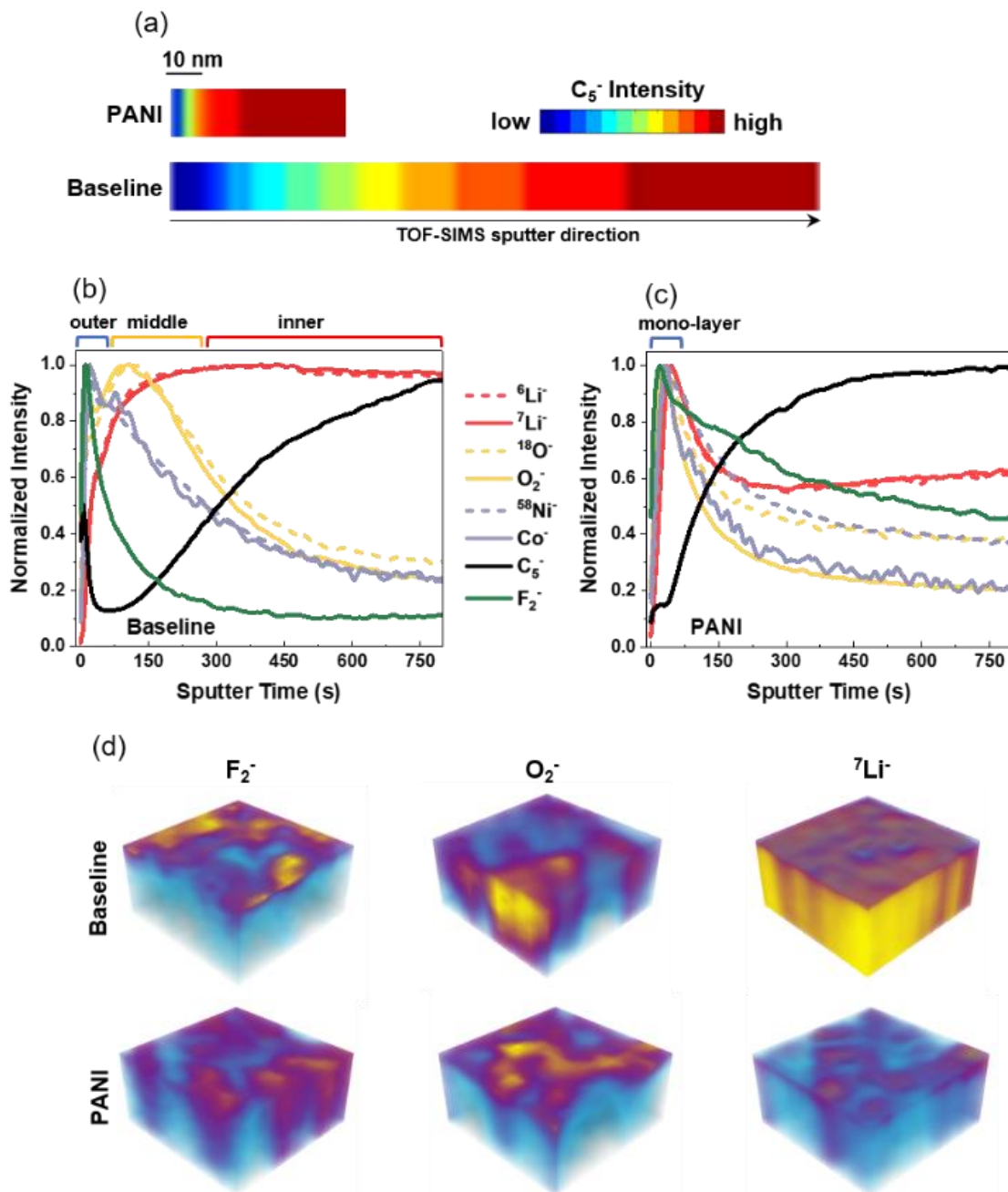
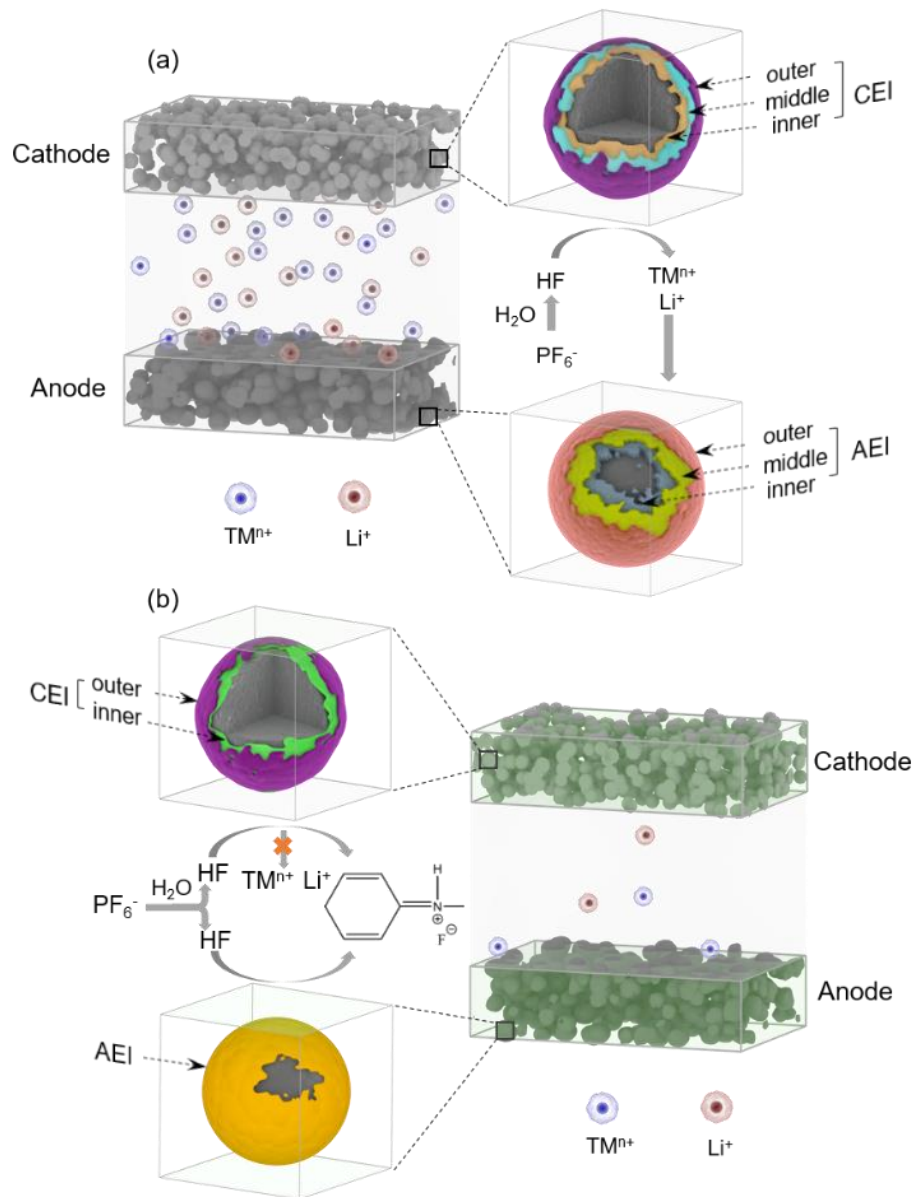


**Figure 4.** (a) Comparison of the TOF-SIMS depth profiles of  $C_5^-$  fragment, and TOF-SIMS depth profiles (normalized to maximum) of various fragments of interest on the graphite anodes retrieved from 1,000 cycled full cells with (b) baseline and (c) PANI binders. (d) Corresponding 3D distribution of representative interphasial species in the TOF-SIMS sputtered volume ( $100\ \mu\text{m}$  (length)  $\times$   $100\ \mu\text{m}$  (width)  $\times$   $32\ \text{nm}$  (height)).

ble layer could be created.<sup>26,34</sup> Also, the degree of the peak shift is closely related to the concentration of metallic Li formed.<sup>35</sup> Therefore, a significant amount of metallic Li is deposited on the graphite surface in the baseline sample, which is further verified by the stronger  $^6\text{Li}/^7\text{Li}$  yields in Figure 3e. Additionally, much stronger Ni 2p peaks are detected on the graphite surface in the baseline sample (Figure 3d), which is consistent with the higher  $^{58}\text{Ni}$  yield as shown in Figure 3e, indicating considerable transition-metal deposition on the graphite surface upon cycling. Figure 3f and 3g provide a more quantitative comparison of the total yields of transition-metal and Li-related species, both of which in the PANI sample are nearly one order of

magnitude lower than that in the baseline sample. It confirms much less active Li trapping and transition-metal deposition on graphite with the PANI binder framework due to the greatly alleviated cathode surface reactivity, accompanied by much less electrolyte decomposition (represented by  $C_2O^-$  and  $C_2HO^-$ , Figure 3e) during prolonged cycling.

It is interesting to note that the deposited transition-metal fragments on the graphite surface are not in pure metallic state, as they are partially fluorinated (represented by  $^{58}\text{NiF}^-$ ) or oxidized (represented by  $^{58}\text{NiO}^-$ ) (Figure 3h). All the transition-metal species show stronger intensities in the baseline sample. Similarly, the fluorinated Li (represented by  $^7\text{LiF}_2^-$ ) and oxidized Li species (represented by  $^7\text{LiO}^-$ ) are



**Scheme 1.** Schematic illustrations of the interphasial evolution process for the full cells with (a) baseline and (b) PANI binders in the electrodes.

also detected on the graphite surface (Figure 3i). As expected, the baseline sample shows much stronger  ${}^7\text{LiO}^-$  yield; the  ${}^7\text{LiF}_2^-$  intensity, however, is much weaker in this case. It suggests the fluorinated Li is not continuously formed as the active Li is being trapped on graphite. Instead, it is mainly generated during  $\text{LiPF}_6$  decomposition to form the AEI at early cycling stages, and the fluorinated Li could contribute to a robust interphase for anode protection.<sup>36</sup> Hence, the continuous loss of fluorinated Li in the baseline sample upon prolonged cycling results in a more vulnerable AEI on the graphite anode.

Like the CEI, the AEI thickness varies significantly in different binder systems, and it can be estimated by the TOF-SIMS sputtering depth, where  $\text{C}_5^-$  reaches its maximum intensity.<sup>3</sup> As shown in Figure 4a, the AEI in the baseline sample (130 nm) is  $\sim 6$  times thicker than that of the PANI sample (20 nm) after 1,000 cycles. Furthermore, the AEI exhibits heterogeneous chemical characteristics where the interphasial species comprise a layered microstructure.<sup>3</sup> For the

baseline sample in Figure 4b, the AEI features a thick triple-layer architecture, where F-enriched (represented by  $\text{F}_2^-$ ) and transition-metal species (represented by  ${}^{58}\text{Ni}/\text{Co}^-$ ) dominate the exterior layer, O-enriched species (represented by  ${}^{18}\text{O}^-/\text{O}_2^-$ ) comprise the intermediate layer, and Li-enriched species (represented by  ${}^6\text{Li}/{}^7\text{Li}^-$ ) penetrate the interior layer of the AEI. In sharp contrast, the AEI in the PANI sample manifests a thin mono-layer architecture (Figure 4c), where all the interphasial species reside on the very surface of the AEI. The 3D distribution of TOF-SIMS fragments in Figure 4d gives a more straightforward illustration on the microstructure variation. As demonstrated, for the baseline sample,  $\text{F}_2^-$ ,  $\text{O}_2^-$ , and  ${}^7\text{Li}^-$  fragments demonstrate distinct spatial distribution in the AEI, residing, respectively, in the exterior, intermediate, and interior layers of AEI. For the PANI sample, however, the dominant regions of  $\text{F}_2^-$ ,  $\text{O}_2^-$ , and  ${}^7\text{Li}^-$  nearly overlap with each other, maintaining a mono-layer structure after 1,000 cycles.

Based on above XPS and TOF-SIMS analyses, the correlation between the cathode surface reaction and the interphasial chemical evolution on both electrode sides is illustrated in Scheme 1a. During a typical cycling process, the ultrahigh-Ni layered oxide reacts aggressively with carbonate electrolyte, causing CEI thickening with a complex triple-layer interphasial architecture. Subsequently, a significant amount of active material (including Li, transition-metal ions) is dissolved from the cathode side, which would deposit on the anode surface through a dissolution, migration, and deposition (DMD) process and damage the AEI integrity.<sup>37</sup> Consequently, the AEI goes through a continuous destruction-reconstruction process, where electrolyte and Li ions suffer from irreversible consumption.<sup>38</sup> Eventually, the AEI degrades to a thick, vulnerable triple-layer structure. However, benefiting from the PANI binder framework that effectively tunes the cathode surface chemistry and scavenges the acidic species in the electrolyte, the cathode surface reaction as well as the active-material dissolution can be greatly alleviated (Scheme 1b). The CEI is thereby tuned to be a more robust, thinner dual-layer chemical architecture. Also, the graphite anode is free from severe chemical abuse, exhibiting a well-maintained thin mono-layer architecture upon extensive cycling.

### 3. CONCLUSIONS

In summary, a conductive and acid-scavenging binder framework incorporating a p-type polymer PANI is established and applied to the ultrahigh-Ni layered oxide system ( $\text{LiNi}_{0.94}\text{Co}_{0.06}\text{O}_2$ ). On one hand, the conductive PANI binder system helps facilitate electron transfer and improve the rate capability of the electrode even at low temperatures ( $-20\text{ }^\circ\text{C}$ ). On the other hand, by scavenging the acidic species through a protonation effect of PANI, the cathode surface chemistry is effectively optimized. Also, the cathode active-material dissolution-migration-deposition process is significantly mitigated, contributing to a more robust, thinner CEI and AEI during repeated cycling. As a result, the capacity retention of the ultrahigh-Ni layered oxide ( $\text{LiNi}_{0.94}\text{Co}_{0.06}\text{O}_2$ ) is greatly improved from 47% to 81% after 1,000 cycles. This work highlights the potential of rational binder optimization for the development of high-energy-density Li-ion batteries.

### 4. EXPERIMENTAL SECTION

**Synthesis of  $\text{LiNi}_{0.94}\text{Co}_{0.06}\text{O}_2$ .** The  $\text{Ni}_{0.94}\text{Co}_{0.06}(\text{OH})_2$  precursors were synthesized through a coprecipitation method. In a typical batch, a mixed solution of  $\text{NiSO}_4 \cdot 6\text{H}_2\text{O}$  (technical grade, Fisher Chemical) and  $\text{CoSO}_4 \cdot 7\text{H}_2\text{O}$  (99+%, Acros Organics) (94 : 6 by molar, 2 M) was continually pumped into a 10 L tank reactor, together with separate feeds of a solution containing 8 M KOH (Certified ACS, Fisher Chemical) and a proper amount of  $\text{NH}_4\text{OH}$  (Certified ACS Plus, 28 – 30%, Fisher Chemical). Reaction condition parameters including the stirring rate, pH ( $\sim 11$ ), and temperature ( $\sim 50\text{ }^\circ\text{C}$ ) were carefully controlled during the whole precipitation. The as-synthesized powder was vacuum filtered, washed, and dried in an oven overnight at  $100\text{ }^\circ\text{C}$  before use. The  $\text{Ni}_{0.94}\text{Co}_{0.06}(\text{OH})_2$  precursor was then mixed with  $\text{LiOH} \cdot \text{H}_2\text{O}$  (98+%, Alfa Aesar) in 1 : 1.03 molar ratio and calcinated at  $640\text{ }^\circ\text{C}$  with oxygen flow for 15 h to yield  $\text{LiNi}_{0.94}\text{Co}_{0.06}\text{O}_2$ . The morphology of the as-prepared

$\text{LiNi}_{0.94}\text{Co}_{0.06}\text{O}_2$  is shown in Figure S10 (Supporting Information).

**Synthesis of Polyaniline (PANI).** In a typical synthetic process, 14.88 g of aniline monomer ( $\geq 99.5\%$ , Sigma Aldrich) was added to 300 mL of 1 M HCl solution (37%, ACS Reagent, Sigma Aldrich) in an ice bath. 9.128 g of ammonium peroxydisulfate ( $\geq 99.5\%$ , Sigma Aldrich) was dissolved in 50 mL of 1 M HCl solution and then gradually dropped into the aniline monomer solution, followed by stirring for 4 h in an ice bath during the whole polymerization. The reaction product was filtered, washed with water, and deprotonated in 1.2 M  $\text{NH}_4\text{OH}$  solution for 4 h. Finally, the as-synthesized powder was vacuum filtered, washed with water several times, and dried in a vacuum oven before use.

**Material Characterization.** The crystal structure was analyzed with X-ray diffraction (XRD) (Rigaku, Miniflex 600,  $1^\circ \text{min}^{-1}$ ). The surface morphology was characterized with a field-emission scanning electron microscope (SEM, Quanta 650). X-ray photoelectron spectroscopy (XPS) measurement was carried out with an Axis Ultra DLD spectrometer (Al  $\text{K}\alpha$  radiation). Time-of-flight secondary ion mass spectrometry (TOF-SIMS) characterization was performed with a TOF.SIMS 5 spectrometer (ION-TOF GmbH). A pulsed  $\text{Bi}_1^+$  (30 eV, 20 ns) ion beam in a high current mode was applied for depth profiling and a  $\text{Cs}^+$  ion (500 eV) beam was utilized for surface analysis. The typical analyzed area was  $100\text{ }\mu\text{m} \times 100\text{ }\mu\text{m}$ . An air-tight interface equipment was used to transfer the air-sensitive samples from an argon-filled glovebox into the XPS or TOF-SIMS instrument, in order to eliminate air contamination during the characterization process. A Leica TIC 020 milling system was adopted to prepare the cross-section cathode.

**Electrochemical Test.** The cathode slurry was prepared by mixing the active material ( $\text{LiNi}_{0.94}\text{Co}_{0.06}\text{O}_2$ ), Super P conductive carbon (MTI Corp.), and binder in a weight ratio of 8 : 1 : 1 in N-methyl-2-pyrrolidone (NMP, 99%, Sigma Aldrich) under vigorous stirring. The baseline binder is bare poly(vinylidene) fluoride (PVDF) (HSV900,  $\geq 99.5\%$ , MTI Corp.), while for the PANI binder, the PANI powder was mixed with PVDF (PVDF : PANI = 5 : 1 by weight). The well-dispersed slurry was cast onto an aluminum foil with an active-material loading of  $\sim 8\text{ mg cm}^{-2}$ . The obtained electrode was dried, calendared, and stored in a vacuum oven before use. The graphite anode slurry was prepared by dispersing the mesocarbon microbead (MCMB) graphite (MTI Corp.), KS-6 synthetic graphite (TIMRES Corp.), Super P conductive carbon, and binder (the baseline or PANI binder) in a weight ratio of 85 : 2.5 : 2.5 : 10 in NMP under vigorous stirring. The obtained slurry was cast onto a copper foil and dried before use. CR2032-type coin cells with lithium-metal chip as the counter electrode and  $\text{LiNi}_{0.94}\text{Co}_{0.06}\text{O}_2$  as the working electrode were assembled inside an argon-filled glovebox ( $\text{H}_2\text{O} < 0.1\text{ ppm}$ ,  $\text{O}_2 < 0.1\text{ ppm}$ ) for half-cell test. The pouch-type full cells were assembled by pairing the  $\text{LiNi}_{0.94}\text{Co}_{0.06}\text{O}_2$  cathode and the graphite anode with a N/P ratio of  $\sim 1.1$ . The electrolyte contained 1 M  $\text{LiPF}_6$  in ethylene carbonate (EC) : ethyl methyl carbonate (EMC) (3 : 7 by weight) (Gotion Corp.) with 2 wt.% vinylene carbonate (VC, 99.5%,  $\text{H}_2\text{O} < 10\text{ ppm}$ , Sigma Aldrich) as an additive. For the half-cell cycling test, two formation cycles at C/10 rate were performed, followed by cycling at C/3 rate at 2.8 – 4.4 V vs  $\text{Li/Li}^+$ . For the

full-cell cycling test, two formation cycles at C/10 rate was conducted before the long-term cycling at C/2 rate at 2.7 – 4.3 V.  $1C = 180 \text{ mA g}^{-1}$ . The calculated voltage hysteresis is defined as the difference between the average charge and discharge voltages. The Linear sweep voltammetry test on the cathode electrode was conducted in half cells where no separator or electrolyte was added but stainless steel was adopted as the counter electrode.

## ASSOCIATED CONTENT

**Supporting Information.** Additional electrochemical test result (charge/discharge curves, Coulombic efficiency, cycling performance, discharge voltage vs. cycle number curve), SEM images, XPS data, Rietveld refinement result and statistic summary of TM fragments, Li fragments from TOF-SIMS.

## AUTHOR INFORMATION

### Corresponding Author

\* E-mail: manth@austin.utexas.edu

### Notes

The authors declare no competing financial interest.

## ACKNOWLEDGMENT

This work was supported by the Assistant Secretary for Energy Efficiency and Renewable Energy, Office of Vehicle Technologies of the U.S. Department of Energy through the Advanced Battery Materials Research (BMR) Program (Battery500 Consortium) award number DE-EE0007762 and the Welch Foundation grant F-1254. The author also thanks Dr. Hugo Celio for assistance with XPS characterization, Dr. Andrei Dolocan for assistance with TOF-SIMS characterization, Ms. Liu Luo for assistance with manuscript revision.

## REFERENCES

- (1) Manthiram, A., An Outlook on Lithium-Ion Battery Technology. *ACS Cent. Sci.* **2017**, *3*, 1063-1069.
- (2) Gauthier, M.; Carney, T. J.; Grimaud, A.; Giordano, L.; Pour, N.; Chang, H. H.; Fenning, D. P.; Lux, S. F.; Paschos, O.; Bauer, C.; Maglia, F.; Lupart, S.; Lamp, P.; Shao-Horn, Y., Electrode-Electrolyte Interface in Li-Ion Batteries: Current Understanding and New Insights. *J. Phys. Chem. Lett.* **2015**, *6*, 4653-72.
- (3) Li, J.; Li, W.; You, Y.; Manthiram, A., Extending the Service Life of High-Ni Layered Oxides by Tuning the Electrode-Electrolyte Interphase. *Adv. Energy Mater.* **2018**, *8*, 1801957.
- (4) Manthiram, A.; Song, B.; Li, W., A Perspective on Nickel-Rich Layered Oxide Cathodes for Lithium-Ion Batteries. *Energy Storage Mater.* **2017**, *6*, 125-139.
- (5) Yan, P.; Zheng, J.; Liu, J.; Wang, B.; Cheng, X.; Zhang, Y.; Sun, X.; Wang, C.; Zhang, J.-G., Tailoring Grain Boundary Structures and Chemistry of Ni-Rich Layered Cathodes for Enhanced Cycle Stability of Lithium-Ion Batteries. *Nat. Energy* **2018**, *3*, 600-605.
- (6) Yan, P.; Zheng, J.; Chen, T.; Luo, L.; Jiang, Y.; Wang, K.; Sui, M.; Zhang, J. G.; Zhang, S.; Wang, C., Coupling of Electrochemically Triggered Thermal and Mechanical Effects to Aggravate Failure in a Layered Cathode. *Nat. Commun.* **2018**, *9*, 2437.
- (7) Oh, P.; Oh, S. M.; Li, W.; Myeong, S.; Cho, J.; Manthiram, A., High-Performance Heterostructured Cathodes for Lithium-Ion Batteries with a Ni-Rich Layered Oxide Core and a Li-Rich Layered Oxide Shell. *Adv. Sci.* **2016**, *3*, 1600184.
- (8) Zou, L.; Liu, Z.; Zhao, W.; Jia, H.; Zheng, J.; Yang, Y.; Wang, G.; Zhang, J.-G.; Wang, C., Solid-Liquid Interfacial Reaction Triggered Propagation of Phase Transition from Surface into Bulk Lattice of Ni-Rich Layered Cathode. *Chem. Mater.* **2018**, *30*, 7016-7026.
- (9) Zou, L.; Zhao, W.; Liu, Z.; Jia, H.; Zheng, J.; Wang, G.; Yang, Y.; Zhang, J.-G.; Wang, C., Revealing Cycling Rate-Dependent Structure Evolution in Ni-Rich Layered Cathode Materials. *ACS Energy Lett.* **2018**, *3*, 2433-2440.
- (10) Li, J.; Li, W.; Wang, S.; Jarvis, K.; Yang, J.; Manthiram, A., Facilitating the Operation of Lithium-Ion Cells with High-Nickel Layered Oxide Cathodes with a Small Dose of Aluminum. *Chem. Mater.* **2018**, *30*, 3101-3109.
- (11) Song, B.; Li, W.; Oh, S. M.; Manthiram, A., Long-Life Nickel-Rich Layered Oxide Cathodes with a Uniform  $\text{Li}_2\text{ZrO}_3$  Surface Coating for Lithium-Ion Batteries. *ACS Appl. Mater. Interfaces* **2017**, *9*, 9718-9725.
- (12) Wang, J.; Du, C.; Yan, C.; Xu, X.; He, X.; Yin, G.; Zuo, P.; Cheng, X.; Ma, Y.; Gao, Y., Role of Fluorine Surface Modification in Improving Electrochemical Cyclability of Concentration Gradient  $\text{Li}[\text{Ni}_{0.73}\text{Co}_{0.12}\text{Mn}_{0.15}]\text{O}_2$  Cathode Material for Li-Ion Batteries. *RSC Adv.* **2016**, *6*, 26307-26316.
- (13) Jiao, S.; Ren, X.; Cao, R.; Engelhard, M. H.; Liu, Y.; Hu, D.; Mei, D.; Zheng, J.; Zhao, W.; Li, Q.; Liu, N.; Adams, B. D.; Ma, C.; Liu, J.; Zhang, J.-G.; Xu, W., Stable Cycling of High-Voltage Lithium Metal Batteries in Ether Electrolytes. *Nat. Energy* **2018**, *3*, 739-746.
- (14) Li, W.; Dolocan, A.; Li, J.; Xie, Q.; Manthiram, A., Ethylene Carbonate-Free Electrolytes for High-Nickel Layered Oxide Cathodes in Lithium-Ion Batteries. *Adv. Energy Mater.* **2019**, *9*, 1901152.
- (15) Zeng, H.; Lu, D.; He, J.; Fang, D.; Liang, Y.; Zhao, R.; Cai, Y., Nano-Sized  $\text{AlPO}_4$  Coating Layer on Graphite Powder to Improve Electrochemical Properties of High Voltage Graphite/ $\text{LiNi}_{0.5}\text{Mn}_{1.5}\text{O}_4$  Li-Ion Cells. *Energy Technol-Ger* **2019**, *7*, 1801078.
- (16) Ryu, K. S.; Jung, J. H.; Joo, J.; Chang, S. H., Improved Conducting States Induced by an Electrochemical Charging Process in Polyaniline Film Doped with New Dopants. *J. Electrochem. Soc.* **2002**, *149*, A478-A482.
- (17) Ryu, K. S.; Kim, K. M.; Kang, S.; Lee, G. J.; Joo, J.; Chang, S. H., Electrochemical and Physical Characterization of Lithium Ionic Salt Doped Polyaniline as a Polymer Electrode of Lithium Secondary Battery. *Synth. Met.* **2000**, *110*, 213-217.
- (18) Xu, J.; Lin, F.; Doeff, M. M.; Tong, W., A Review of Ni-Based Layered Oxides for Rechargeable Li-Ion Batteries. *J. Mater. Chem. A* **2017**, *5*, 874-901.
- (19) Xu, S.; Du, C.; Xu, X.; Han, G.; Zuo, P.; Cheng, X.; Ma, Y.; Yin, G., A Mild Surface Washing Method Using Protonated Polyaniline for Ni-Rich  $\text{LiNi}_{0.8}\text{Co}_{0.1}\text{Mn}_{0.1}\text{O}_2$  Material of Lithium-Ion Batteries. *Electrochim. Acta* **2017**, *248*, 534-540.
- (20) Lin, F.; Markus, I. M.; Nordlund, D.; Weng, T. C.; Asta, M. D.; Xin, H. L.; Doeff, M. M., Surface Reconstruction and Chemical Evolution of Stoichiometric Layered Cathode Materials for Lithium-Ion Batteries. *Nat. Commun.* **2014**, *5*, 3529.

- (21) Boulineau, A.; Simonin, L.; Colin, J. F.; Bourbon, C.; Patoux, S., First Evidence of Manganese-Nickel Segregation and Densification Upon Cycling in Li-Rich Layered Oxides for Lithium Batteries. *Nano Lett.* **2013**, *13*, 3857-63.
- (22) Jung, S.-K.; Gwon, H.; Hong, J.; Park, K.-Y.; Seo, D.-H.; Kim, H.; Hyun, J.; Yang, W.; Kang, K., Understanding the Degradation Mechanisms of  $\text{LiNi}_{0.5}\text{Co}_{0.2}\text{Mn}_{0.3}\text{O}_2$  Cathode Material in Lithium-Ion Batteries. *Adv. Energy Mater.* **2014**, *4*, 1300787.
- (23) Oh, P.; Ko, M.; Myeong, S.; Kim, Y.; Cho, J., A Novel Surface Treatment Method and New Insight into Discharge Voltage Deterioration for High-Performance  $0.4\text{Li}_2\text{MnO}_3\text{-}0.6\text{LiNi}_{1/3}\text{Co}_{1/3}\text{Mn}_{1/3}\text{O}_2$  cathode Materials. *Adv. Energy Mater.* **2014**, *4*, 1400631.
- (24) Bianchini, M.; Roca-Ayats, M.; Hartmann, P.; Brezesinski, T.; Janek, J., There and Back Again-the Journey of  $\text{LiNiO}_2$  as a Cathode Active Material. *Angew. Chem.; Int. Ed.* **2018**, *58*, 10434-10458.
- (25) Li, Y.; Wan, S.; Veith, G. M.; Unocic, R. R.; Paranthaman, M. P.; Dai, S.; Sun, X.-G., A Novel Electrolyte Salt Additive for Lithium-Ion Batteries with Voltages Greater Than 4.7 V. *Adv. Energy Mater.* **2017**, *7*, 1601397.
- (26) Xu, M.; Zhou, L.; Dong, Y.; Chen, Y.; Garsuch, A.; Lucht, B. L., Improving the Performance of Graphite/ $\text{LiNi}_{0.5}\text{Mn}_{1.5}\text{O}_4$  cells at High Voltage and Elevated Temperature with Added Lithium Bis(Oxalato) Borate (Libob). *J. Electrochem. Soc.* **2013**, *160*, A2005-A2013.
- (27) MacDiarmid, A. G.; Epstein, A. J., Polyanilines: A Novel Class of Conducting Polymers. *Faraday Discuss. Chem. Soc.* **1989**, *88*, 317-332.
- (28) He, H.; Hu, Y.; Chen, S.; Zhuang, L.; Ma, B.; Wu, Q., Preparation and Properties of a Hyperbranch-Structured Polyamine Adsorbent for Carbon Dioxide Capture. *Sci. Rep.* **2017**, *7*, 3913.
- (29) Reiter, J.; Nádherná, M.; Dominko, R., Graphite and  $\text{LiCo}_{1/3}\text{Mn}_{1/3}\text{Ni}_{1/3}\text{O}_2$  Electrodes with Piperidinium Ionic Liquid and Lithium Bis(Fluorosulfonyl)Imide for Li-Ion Batteries. *J. Power Sources* **2012**, *205*, 402-407.
- (30) Farhat, D.; Ghamouss, F.; Maibach, J.; Edstrom, K.; Lemordant, D., Adiponitrile-Lithium Bis(trimethylsulfonyl)imide Solutions as Alkyl Carbonate-Free Electrolytes for  $\text{Li}_4\text{Ti}_5\text{O}_{12}$ (LTO)/ $\text{LiNi}_{1/3}\text{Co}_{1/3}\text{Mn}_{1/3}\text{O}_2$  (NMC) Li-Ion Batteries. *Chemphyschem.* **2017**, *18*, 1333-1344.
- (31) Banerjee, A.; Ziv, B.; Shilina, Y.; Luski, S.; Aurbach, D.; Halalay, I. C., Acid-Scavenging Separators: A Novel Route for Improving Li-Ion Batteries' Durability. *ACS Energy Lett.* **2017**, *2*, 2388-2393.
- (32) Goodenough, J. B.; Kim, Y., Challenges for Rechargeable Li Batteries. *Chem. Mater.* **2010**, *22*, 587-603.
- (33) Xu, K., Electrolytes and Interphases in Li-Ion Batteries and Beyond. *Chem. Rev.* **2014**, *114*, 11503-618.
- (34) Oswald, S., Binding Energy Referencing for Xps in Alkali Metal-Based Battery Materials Research (I): Basic Model Investigations. *Appl. Surf. Sci.* **2015**, *351*, 492-503.
- (35) Oswald, S.; Thoss, F.; Zier, M.; Hoffmann, M.; Jaumann, T.; Herklotz, M.; Nikolowski, K.; Scheiba, F.; Kohl, M.; Giebeler, L.; Mikhailova, D.; Ehrenberg, H., Binding Energy Referencing for Xps in Alkali Metal-Based Battery Materials Research (II): Application to Complex Composite Electrodes. *Batteries* **2018**, *4*, 36.
- (36) Xin-bing, C.; Rui, Z.; Chen-Zi, Z.; Qiang, Z., Toward Safe Lithium Metal Anode in Rechargeable Batteries: a Review. *Chem. Rev.* **2017**, *117*, 10403-10473.
- (37) Feng, Z.; Huang, X.; Rajagopalan, R.; Tang, Y.; Peng, Z.; Wang, H., Enhanced Electrochemical Properties of  $\text{LiNi}_{0.8}\text{Co}_{0.1}\text{Mn}_{0.1}\text{O}_2$  at Elevated Temperature by Simultaneous Structure and Interface Regulating. *J. Electrochem. Soc.* **2019**, *166*, A1439-A1448.
- (38) Cheng, X.; Zheng, J.; Lu, J.; Li, Y.; Yan, P.; Zhang, Y., Realizing Superior Cycling Stability of Ni-Rich Layered Cathode by Combination of Grain Boundary Engineering and Surface Coating. *Nano Energy* **2019**, *62*, 30-37.